

**Original citation:**

Reyes-Aldasoro, C. C. and Bhalerao, Abhir (2002) Classification of human knee data from magnetic resonance images. Department of Computer Science. (Department of Computer Science Research Report). (Unpublished) CS-RR-388

**Permanent WRAP url:**

<http://wrap.warwick.ac.uk/61240>

**Copyright and reuse:**

The Warwick Research Archive Portal (WRAP) makes this work by researchers of the University of Warwick available open access under the following conditions. Copyright © and all moral rights to the version of the paper presented here belong to the individual author(s) and/or other copyright owners. To the extent reasonable and practicable the material made available in WRAP has been checked for eligibility before being made available.

Copies of full items can be used for personal research or study, educational, or not-for-profit purposes without prior permission or charge. Provided that the authors, title and full bibliographic details are credited, a hyperlink and/or URL is given for the original metadata page and the content is not changed in any way.

**A note on versions:**

The version presented in WRAP is the published version or, version of record, and may be cited as it appears here. For more information, please contact the WRAP Team at: [publications@warwick.ac.uk](mailto:publications@warwick.ac.uk)



<http://wrap.warwick.ac.uk/>

# Classification of Human Knee Data from Magnetic Resonance Images

Constantino Carlos Reyes-Aldasoro and Abhir Bhalerao

March 2002

Department of Computer Science, The University of Warwick.

## **ABSTRACT**

This report considers the general problem of segmentation of Magnetic Resonance Images. The final objective is to correctly assign a unique label or class which represents an anatomical structure to every pixel or voxel in a data set. The images analysed describe a human knee scanned by Magnetic Resonance (MR). A brief description of the anatomy of the knee and physics of MR imaging is given. A review of image segmentation approaches, focusing on multiresolution and texture segmentation, follows. The first segmentation technique implemented here is grey level thresholding, which is later improved by adding two other descriptors of the images: standard deviation and a moment from the co-occurrence matrix. Frequency analysis through sub-band filtering is proposed as a way to improve the description of the textural regions and boundaries between anatomical regions. Comparative results of the different techniques are presented and finally conclusions and future work is proposed.

**Keywords:** Image Segmentation, Clustering, Classification, Texture.

# Contents

<b>1</b>	<b>INTRODUCTION</b>	<b>1</b>
<b>2</b>	<b>BACKGROUND</b>	<b>2</b>
2.1	Human Knee Joint . . . . .	2
2.2	Magnetic Resonance Imaging and Imaging Technologies . . . . .	2
2.3	Image Segmentation Techniques . . . . .	6
2.4	Multiple Resolution . . . . .	9
2.5	Texture . . . . .	12
<b>3</b>	<b>ANALYSIS OF THE DATA</b>	<b>13</b>
3.1	Grey level thresholding . . . . .	13
3.2	Standard Deviation of the grey level . . . . .	15
3.3	The co-occurrence matrix . . . . .	17
3.4	Bhattacharyya distance . . . . .	20
3.5	A Sub-band Filtering Approach . . . . .	22
<b>4</b>	<b>COMPARATIVE RESULTS</b>	<b>23</b>
<b>5</b>	<b>FUTURE WORK</b>	<b>26</b>
<b>6</b>	<b>CONCLUSIONS</b>	<b>28</b>

## List of Figures

1	A simplified view of a knee joint: anterior and posterior view of leg in extension and anterior view of the leg in flexion. . . . .	3
2	Nuclear Magnetic Resonance. (a) Nuclei in natural equilibrium (b) Nuclei aligned with external magnetic field (c) Oscillation of nuclei due to periodic magnetic field (d) Resonance around direction of field (e) Relaxation process and release of energy (f) Parallel and perpendicular components of the magnetic field. Adapted from [7] . . . . .	5
3	A MR image of a human knee (a) and the Canny edge detection with two different thresholds (b, c). . . . .	9
4	Gaussian Pyramid constructed from a MRI of a Human Knee. Images contain 512x512, 256x256, 128x128, 64x64 and 32x32 pixels. . . . .	11
5	Three different levels of a Laplacian Pyramid constructed from a MR image slice of a human knee. . . . .	12
6	Human Knee Slice MRI: (a) grey level image and (b) its corresponding histogram. . . . .	14
7	Three classes segmented by grey level thresholding: (a) Background, (b) Muscle and (c) Bone/Tissue. . . . .	15
8	(a) Four manually segmented regions: Background, Muscle, Bone and Tissue, and (b) their corresponding histograms. . . . .	16
9	Relative frequencies of grey levels for four different levels of the Gaussian Pyramid presented in figure 4: (a) Level 1 (b) Level 2 (c) Level 3 (d) Level 4. . . . .	18
10	Descriptors of figure 6(a) calculated over an $8 \times 8$ neighbourhood tessellation: (a) Values of Standard Deviation of the pixel intensities (b) Difference moment of order 2 of the co-occurrence matrix. . . . .	19
11	Bhattacharyya distance cases (a) different means with small variances (b) Similar means, different variances. . . . .	20
12	Scatter plots of the four selected sections: background, bone, tissue and muscle (a) Mean - Standard Deviation, (b) Mean - Difference moment of order 2. . . . .	21
13	(a) Primitive tessellation operators and (b) Second orientation pyramid of order 3 for frequency domain tessellation used to analyse the frequency domain (c) Tree description of the regions of the pyramid. . . . .	22
14	Two separate levels of the Second Orientation Pyramid, each containing 13 Regions: (a) first two levels of the Second Orientation Pyramid, regions 2 to 14, (b) third and fourth level, regions 23 to 35. . . . .	24

15	K-means classification of MR image of a human knee based on 9 parameters: mean, standard deviation and difference order moment of order 3 of the co-occurrence matrix of three tessellations of size $4 \times 4$ , $8 \times 8$ and $16 \times 16$ . (a) Four classes represented by intensity values: 1 - background, 2 - muscle, 3 - bone and 4 - tissue. (b) Four classes individually presented.	25
16	K-means classification of MR image of a human knee based on frequency and orientation regions from (a) First level of the Second Orientation Pyramid (b) Second level of the Second Orientation Pyramid (c) Third level of the Second Orientation Pyramid. . . . .	25
17	Error ratio comparison between Frequency domain sub-band filtering and Spatial domain features, co-occurrence matrix, variance and mean. .	26
18	T1, T2 and PD MR Images of a human knee. . . . .	27

## List of Tables

1	Imaging Technologies commonly used for breast cancer screening and diagnosis. . . . .	4
2	Magnetic Resonance; advantages and disadvantages . . . . .	6
3	Mean and variance values for classes and Bhattacharyya distance . . . .	21

# 1 INTRODUCTION

Medical Imaging has seen a huge development in recent years, in particular Magnetic Resonance (MR) has been successfully employed by physicians in diagnosis, quantification and planning of surgery. New applications and techniques for post-processing are being developed constantly and, at a certain level, these new applications require a process of segmentation or classification. This report presents the research done by the author towards a semi-automated segmentation framework for MR data that aims to integrate several methods for segmentation, and provide a way to select and use the most adequate for a given problem. The experiments for the report have been conducted on high resolution Magnetic Resonance images of the human knee joint.

MR Images of a human knee contain many interesting structures: *bone, cartilage, muscle, ligaments*, and the images have the characteristics of *non-uniform intensity, well-defined borders, different textures*. Besides, knee surgery has become a common operation. According to the American Academy of Orthopaedic Surgeons [1], in the United States during 1997 more than 5 million patients visited orthopaedic surgeons with knee problems and 1.4 million were attended in hospital emergency rooms. Of these, about that 4 million were related to injuries and the rest to arthritis and other disorders. By 2000, the number of cases had risen to more than 10 millions visits per year which represents 26% of the cases treated by the orthopaedic surgeons surveyed in [1]. The treatment for the knee problems can range from physiotherapy, to visual examination of the interior of the joint, or arthroscopy, to total knee replacement.

Imaging of the knee and other regions of the body can help physicians in different ways: diagnosis, quantification or intervention. Diagnosis allows the physician to observe the condition of the patient without direct intervention. In other cases, it can prove the presence of a specific feature, a tumour, for instance. Quantification is concerned with measuring or quantifying a certain structure; e.g. the size of a tumour or the thickness of a cartilage. This can be used to determine a therapy and its effectiveness after a certain period of time. In cases of surgical intervention, imaging techniques are used in planning and guidance of the operation, with the objectives of reducing costs and improving the outcome. An ultimate objective of the framework of this work is to provide a symbolic description of the input data, including geometry, function and abnormalities.

The report is organised as follows. Background information about the anatomy of the human knee, Magnetic Resonance imaging and imaging technologies and image segmentation techniques is included in section 2 with two important approaches to segmentation; multiple resolution and texture. Section 3 presents an analysis of the data starting with the grey level description through histogram thresholding. Then, two additional descriptors of the data are presented: variance and co-occurrence description. Sub-band filtering is also analysed. Section 4 presents the comparative results of segmentation with the different techniques. Section 5 presents future work that can be used to improve the present result. Finally, some conclusions are presented.

## 2 BACKGROUND

### 2.1 Human Knee Joint

The knee joint (figure 1) is the most complicated joint in the human body [10], and it is inherently unstable. This condition leads to several injuries and problems like torn meniscus, tendon rupture, and patellar or cruciate ligaments problems, among many others. The knee articulation joins the femur, which has large medial and lateral condyles, with the tibia that has small and shallow condyles. The condyles of the tibia are deepened by crescent shaped rims of fibrocartilage, also called menisci. The knee joint is surrounded by a fibrous capsule that encloses articulations between tibia, femur, fibula and the patella, a thin bone in front of the knee. The joint is strengthened by several ligaments. At the sides, fibular and tibial collateral ligaments prevent side to side movements and add strength while the leg is straight. In the front, the strength is given by the tendon of quadriceps femoris and the patella. In the back, oblique popliteal ligament prevent over extension. In the inner part, the cruciate ligaments, anterior and posterior, limit the rotation and the forward and backward motion of the tibia.

The knee joint has two natural movements of *roll* back and forth or the ordinary flexion - extension. This movement, in which the femoral condyles roll over the menisci starts with the muscles of thigh and calf touching at approximately  $40^\circ$ , up to  $165^\circ$ , almost full extent of the leg. From  $165^\circ$  to  $180^\circ$  with the foot firmly upon the ground, the rolling ceases and the femur rotates medially and *glides* backwards in a locking mechanism when the flexion - extension of the leg is accomplished.

### 2.2 Magnetic Resonance Imaging and Imaging Technologies

Magnetic Resonance Imaging (MRI) is one of the several techniques used for imaging the Human Body. These techniques focus on obtaining images of different structures of the human body with good accuracy, without the direct surgical intervention. Historically, the first imaging technique is the X-rays discovered by Röntgen in which a film records the attenuation presented by different tissues of the body at the exposure to electromagnetic radiation of very high frequency. The resulting image presents shadows of the structures along the path of the rays.

Since the discovery of X-rays, many different techniques to obtain images from the human body have been developed relying on the use of electromagnetic radiation; microwaves, gamma rays or infrared, sound waves, magnetic fields, sub-atomic particles, or electron beams. Table 1 presents some imaging technologies commonly used today [31].

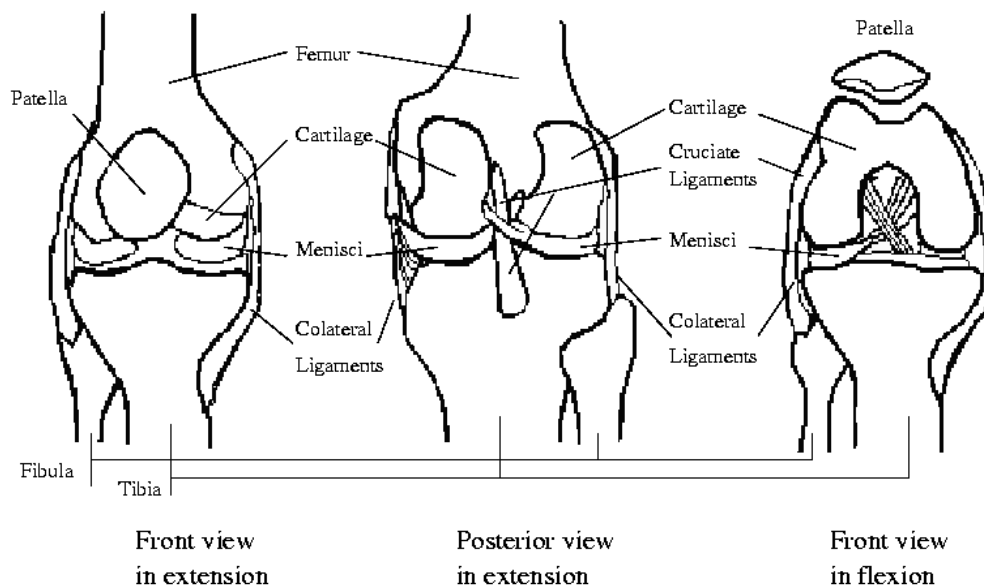


Figure 1: A simplified view of a knee joint: anterior and posterior view of leg in extension and anterior view of the leg in flexion.

Magnetic Resonance Imaging is a powerful method of non-invasive imaging of the interior of a living body for medical diagnostic and other purposes [19]. The underlying principle of MRI is that the nuclei of certain atoms have the property of spin and absorb radio waves of a strictly defined frequency when placed in a magnetic field. The atom of hydrogen presents the magnetic resonance effect, and is abundant in the human body in molecules of water. Most MRI is focused on hydrogen, which constitutes around 63% of the human body [15]. However, other atoms not so abundant in the body, such as phosphorus or sodium can be used to form images.

When atoms are placed in a magnetic field  $\vec{B}$ , the nuclei align with or against the field (See figure 2 a, b). Then, a second field, periodic at a certain precession frequency of the atoms, forces them to oscillate around the fixed magnetic field (c). The nuclei have absorbed energy, and oscillate at a frequency proportional to the intensity of the magnetic field (d). This energy is then released (e) over a certain period of time in the process of relaxation towards the original state of the atom. The time of relaxation is specific for the nature of the nuclei. During the return to their state of equilibrium, the nuclei release the energy in form of waves. RF coils are placed around the body that is being imaged, and register both the energy and the time of release and from these data, the image is reconstructed [19]. The relaxation of the atoms to their initial state is governed by two physical nuclear processes related to the components of the orientation, one parallel to the magnetic field that takes a time  $T_1$ , and one perpen-

Film-screen X-ray	Standard X- ray technique.
Digital X-ray	Digital version of X-ray technique.
Ultrasound	Forms image by reflection of MegaHertz frequency sound waves.
Magnetic Resonance Imaging	Forms images using radio emissions from nuclear spins.
Scintillation	Senses gamma-ray emission of radio active pharmaceuticals.
Thermography	Seeks from infrared signature.
Electrical impedance imaging	Maps impedance with low-voltage signal.
Optical imaging	Measures scattered near-infrared light.
Electrical potential measurements	Measures potentials at array of detectors on skin.
Positron Emission Tomography	Forms images using emission from annihilation of positrons from radioactive pharmaceuticals.
Novel ultrasound	Compound imaging, 3-D and Doppler imaging.
Elastography	Uses sound or MRI to infer mechanical properties of tissue.
Magnetic Resonance Spectroscopy	Analyses tissue's chemical makeup using radio emissions from nuclear spins.
Thermoacoustic Computed Tomography	Generates short sound pulses using RF pulses and constructs 3-D images from them.
Microwave imaging	Uses scattered microwaves.
Hall-effect imaging	Picks up vibrations of charged particles exposed to a magnetic field.
Magneto-mammography	Senses magnetic contrast agents collected in tumours.

Source: IEEE Spectrum [31]

Table 1: Imaging Technologies commonly used for breast cancer screening and diagnosis.

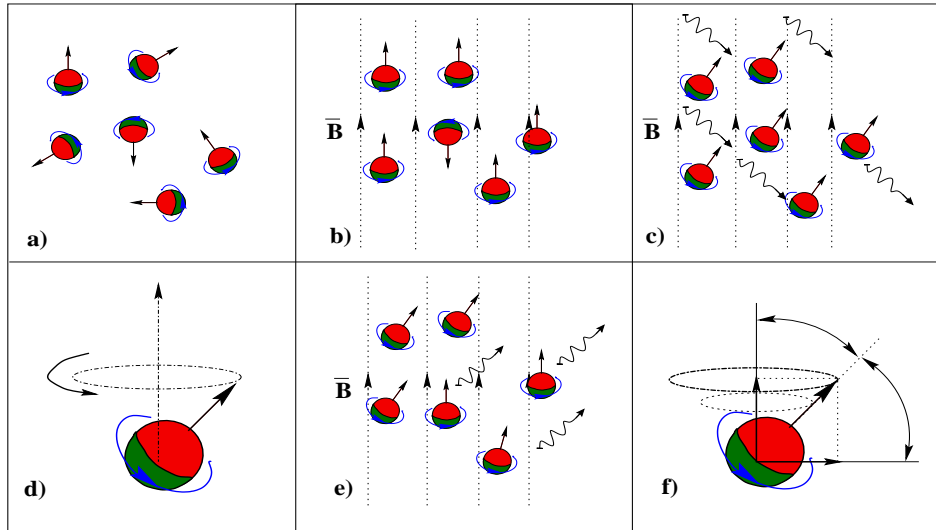


Figure 2: Nuclear Magnetic Resonance. (a) Nuclei in natural equilibrium (b) Nuclei aligned with external magnetic field (c) Oscillation of nuclei due to periodic magnetic field (d) Resonance around direction of field (e) Relaxation process and release of energy (f) Parallel and perpendicular components of the magnetic field. Adapted from [7]

dicular to the field in time T2 (f). These two parameters related with time, in addition to the number of protons that have aligned and are releasing energy contained in a tissue, determine the intensity of the magnetic resonance image intensity. The contrast of the image will depend on the relation of these three parameters. If the number of the protons is the only parameter considered, a Proton density (PD) image is obtained.

The resulting image for the MRI process looks like an internal slice or cut of the body. It is similar to the output of a Computed Tomography (CT) image, but there are substantial differences between them. CT uses X-rays, which are absorbed by the bones, therefore, some regions surrounded by bone are better imaged by MRI than CT. Feeney [14] considers that MRI is the best imaging technique for detecting tumours within the brain stem since bone does not obstruct the imaging. Table 2 presents some advantages and disadvantages of MRI. For more information on this subject Webb [13] has one Chapter for MRI, Hennel [19] is a good introduction and Hornak [20] is a very complete on-line reference. La Recherche [7] has an introductory explanation of magnetism. The Whole Brain Atlas [23] is an on-line atlas with T1, T2 and Proton Density (PD) images of a human brain.

<b>Advantages</b>
Non-ionising radiation. No known physiological side effects.
High soft-tissue contrast. Differences between normal and abnormal tissues.
Any arbitrary slice of organ can be imaged.
Visualisation of areas deep within bony structures; vertebral canal, skull and cerebrospinal fluid.
Natural sources of contrast.
Good for angiography, imaging blood flow without catheters or contrast agents.
3D imaging through computer manipulation of successive slices.
<b>Disadvantages</b>
High cost of equipment.
Claustrophobia of patients.
Long imaging time.
Strong magnetic field; unsuitable for patients with metal implants especially pace makers.
Images distorted by surgical clamps, wire or surgical stitches.
Unable to image calcium; tissue calcification can not be detected.
Acoustic noise; high levels of noise during scanning.

Source: Hennel [19]

Table 2: Magnetic Resonance; advantages and disadvantages

### 2.3 Image Segmentation Techniques

There are many algorithms and techniques used to segment images. Pal [33] considers segmenting as

a process of partitioning an image into non-intersecting regions such that each region is homogeneous and the union of no two homogeneous regions is homogeneous.

For medical imaging, Kapur [22] is more specific regarding segmentation as

a labelling process in which the objective is to assign to each voxel in an image, a unique label which represents an *anatomical structure*.

Segmentation is clearly essential, important and yet a difficult problem in image processing. Suri [37] considers that the shape recovery of medical organs is harder than other computer vision and imaging fields problems, because of large shape variability, structure complexity, artifacts and limitation of body scanning methods. The numerous methods presented in the literature show that there is not one technique that can segment every image. A brief review follows [33, 34].

Rosenfeld [34] categorises segmentation techniques into those which use *statistical* models that describe the pixels in an image and those with *spatial* models that decompose the image into regions. The first use only grey level histograms or grey level probability densities in different order models. The latter assumes that an image

is composed of homogeneous regions and some knowledge of the regions: size, region boundaries or number of regions is required.

Pal categorises segmentation methods into: **grey level thresholding, iterative pixel classification, surface based segmentation, segmentation of colour images, edge detection and methods based on fuzzy set theory.**

One simple and popular segmentation technique is **grey level thresholding**, which can be either based on global (all the image) or local information. In each scheme a single or multiple thresholds for the grey levels can be assigned. The philosophy is that pixels with a grey level  $\leq x$  belong to one region and the remaining pixels to other region. In any case the idea is to partition into regions, *object/background*, or *object<sub>a</sub>/object<sub>b</sub>/...background*. The thresholding methods rely on the assumption that the objects to segment are distinctive in their grey levels and use the histogram information, thus ignoring spatial arrangement of pixels. Although in many cases good results can be obtained, in the particular case of MR images, the intensities of certain structures are often not uniform due to inhomogeneities of the magnets and therefore simple thresholding can divide a single structure into different regions. Another matter to consider is the noise intrinsic to the images that can lead to a misclassification. In many cases the optimal selection of the threshold is not a trivial matter.

Another technique for segmentation is **Iterative Pixel Classification**. This methods rely on the spatial interrelation of the pixels with its neighbours. Markov Random Fields (MRF), Gibbs Random Fields (GRF), probabilistic relaxation and neural networks methods consider the features or characteristic of a pixels as well as a certain neighbourhood of pixels. Energy functions, compatibility measures or training of networks determine the classification. In particular MRF [18, 25, 42] have been widely used in the classification of medical images with good results.

**Surface based segmentation** considers that the image exhibits surface coherence and therefore any kind of image can be modelled as a noisy sample of eight surface primitives: peak, pit, ridge, saddle, ridge, valley, saddle valley, flat and minimal. These techniques are mostly related to range image segmentation and as MR images represent histological cuts or 2-D surfaces the techniques may not be applicable.

**Colour images** contain important information about the perceptual phenomenon of colour related to the different wavelengths of visible electromagnetic spectrum. In many cases, the information is divided into three primary components Red, Green and Blue or psychological qualities hue, saturation and intensity. Prior knowledge of the objects colour can lead to classification of pixels but this is not always known. Segmentation can be performed in the three different fields and the results merged into one segmented image. Although MR images do not contain colour information, a set of T1, T2 and PD images obtained from the same knee at the same session, could provide information in three different ranges of intensity, and then a colour equivalent algorithm could be used.

**Edge detection** consists in detecting abrupt changes in the grey level intensities of the images and interpret them as edges of certain objects. The edges are deter-

mined by local information and can overcome problems of non-uniformity mentioned previously for MR images. There are many methods in the literature that use different approaches, like parallel differential operators such as Roberts, Sobel and Prewitt gradients or Laplacian operator. The operators respond differently to vertical, horizontal, or diagonal edges, corners, lines or isolated points. An important parameter to consider is noise immunity. Marr and Hildreth [29] propose the Laplacian of Gaussian as the best operator; it is differential and it can be tuned at any scale to detect both sharp and blurry edges. If the images are immersed in additive, white Gaussian noise, and antisymmetric features, step or ramp edges, are to be detected, then Canny's algorithm [5] is a major contribution to edge detection. To this date, his paper has more than 500 scientific citations [32]. According to Canny, an edge detector should comply with three criteria: good signal to noise ratio, good locality and small number of false edges. The Canny method looks for local maxima of the gradient of intensity input image. This gradient is approximated from convolutional filters by the derivative of a Gaussian filter. A double threshold is used to detect strong and weak edges. Weak edges are only included if they are connected to strong edges. These thresholds are important in the determination of the edges. Figure 3 (b, c) show two results of edge detection of a Magnetic Resonance image of a human knee. Some interesting properties of the zero-crossings can be observed. On the lower stages, the number of zero-crossings is very high as the noise of the image tends to create zero-crossings. As it is expected, as the stage rises, the number of crossings decrease. On the other hand, as the level increases, the shape can become slightly distorted. As the figure shows, the zero-crossings alone are not sufficient to provide an accurate segmentation of the image, but these zero-crossings could be incorporated into the previous results to delimit the regions described by texture or other methods. Edge detection is a technique that can be used to complement any MR image segmentation procedure.

Finally, **methods based on fuzzy set theory** rely on the idea that imprecise knowledge can be used to define an event. The uncertainties that can arise from imprecise or incomplete information (such as regions not perfectly defined) can be handled by fuzzy set theory. Many algorithms have been proposed for fuzzy clustering, fuzzy thresholding and fuzzy edge detection, and it may be interesting to apply some of these for MR images.

Adaptive Segmentation is proposed by Wells [38] as a new method that overcomes problems of intensity based classification by using the Expectation Maximisation algorithm and knowledge of the tissue intensity and intensity inhomogeneities to correct and segment MR images. More recently, Suri [37] divides the techniques used for 2-D brain segmentation in: **Unsupervised**: Atlas based, Edge based, Probability based, Cluster based, Texture based, Knowledge based, Neural Network based; and **Supervised**: Parametric and Geometric. The author considers that the deformation techniques have had major success and proposes the fusion of geometric and fuzzy clustering as a combination of the supervised and unsupervised methods as *the so-called state-of-the art method*. The fusion of parametric techniques with other techniques

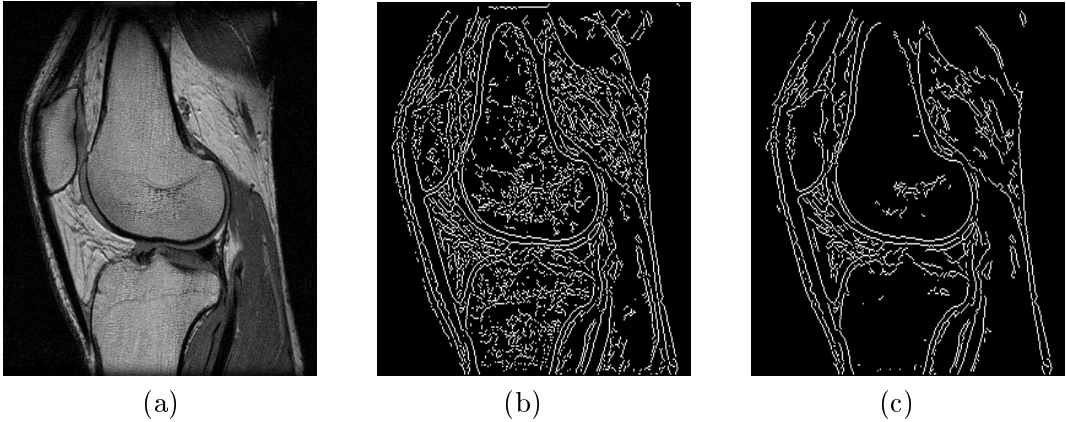


Figure 3: A MR image of a human knee (a) and the Canny edge detection with two different thresholds (b, c).

is also proposed. From this article the idea of a combination of techniques is very important in order to propose a new and powerful method.

## 2.4 Multiple Resolution

An amount of research has been conducted in multiple resolution or multiple scale analysis (for example [26]). In Medical Image Processing, as well as in many other disciplines, the significance or importance of a certain structure will depend on the scale or resolution at which it is being observed. Resolution can determine if the structures in an image are cells, tissues, organs or limbs, it is a variation of the classical problem of observing the tree or observing the forest. The pixels in the image define the level of detail, and, in most cases, the neighbouring pixels are highly correlated and then some information is redundant. By averaging and smoothing the pixel values the image pixels are decorrelated, and the spatial definition is reduced into a new coarser image. By removing detail, further processing on the coarser images is simplified as coarser images have generally less information. Noise present in the image is smoothed and unnecessary detail can be suppressed. One method of observing an image at multiple scales is by the construction of a *pyramid*. As proposed by Burt and Adelson [3], a Gaussian pyramid is constructed by successive levels in which the pixels are weighted and averaged up to the next level giving a low pass filtering effect.

Let the original image  $\mathcal{I}$  have dimensions for rows and columns  $N_r \times N_c$ . Let  $L_c = 1, 2, \dots, N_c$  and  $L_r = 1, 2, \dots, N_r$  be the horizontal and vertical spatial domains, and  $G = 1, 2, \dots, N_g$  the set of grey tones. The image  $\mathcal{I}$  can be represented the as a function that assigns a grey tone to each pair of coordinates:

$$L_r \times L_c; \mathcal{I} : L_r \times L_c \rightarrow G \quad (1)$$

Let the original image  $\mathcal{I}$  be considered as the bottom level of the Gaussian pyramid  $g_0$ . The first level,  $g_1$  is obtained through a low pass filter or reduction of  $g_0$ . For every level, the superior will be obtained then:

$$g_k = REDUCE(g_{k-1}) \quad (2)$$

Each node  $i, j$  of the higher level is a weighted average of the values of the lower level within a  $5 \times 5$  window  $w(m, n)$ :

$$g_k(i, j) = \sum_{m=-2}^2 \sum_{n=-2}^2 w(m, n) g_{k-1}(2i + m, 2j + n) \quad (3)$$

The weights assigned to the nodes within the window are determined by a generating kernel defined by the following constraints:

$$\begin{aligned} w(m, n) &= \hat{w}(m)\hat{w}(n) \\ \sum_{m=-2}^2 \hat{w}(m) &= 1 \\ \hat{w}(i) &= \hat{w}(-i) \end{aligned} \quad (4)$$

which are satisfied when:

$$\begin{aligned} \hat{w}(0) &= a \\ \hat{w}(-1) &= \hat{w}(1) = \frac{1}{4} \\ \hat{w}(-2) &= \hat{w}(2) = \frac{1}{4} - \frac{a}{2} \end{aligned} \quad (5)$$

When  $a = 0.4$  the kernel has a Gaussian-like shape. The effect of the filtering will reduce by half the number of nodes in the image.

The reverse of the function *REDUCE* is *EXPAND* which interpolates new node values between given values. Let  $g_{k,n}$  be the result of expanding  $n$  times  $g_k$ . Then

$$g_{k,n} = EXPAND(g_{k,n-1}) \quad (6)$$

Each node  $i, j$  of the higher level is a weighted average of the values of the lower level within a  $5 \times 5$  window  $w(m, n)$ :

$$g_{k,n}(i, j) = 4 \sum_{m=-2}^2 \sum_{n=-2}^2 w(m, n) g_{k,n-1}\left(\frac{i-m}{2}, \frac{j-n}{2}\right) \quad (7)$$

Figure 4 show a Gaussian pyramid constructed from a MR image of a human knee.

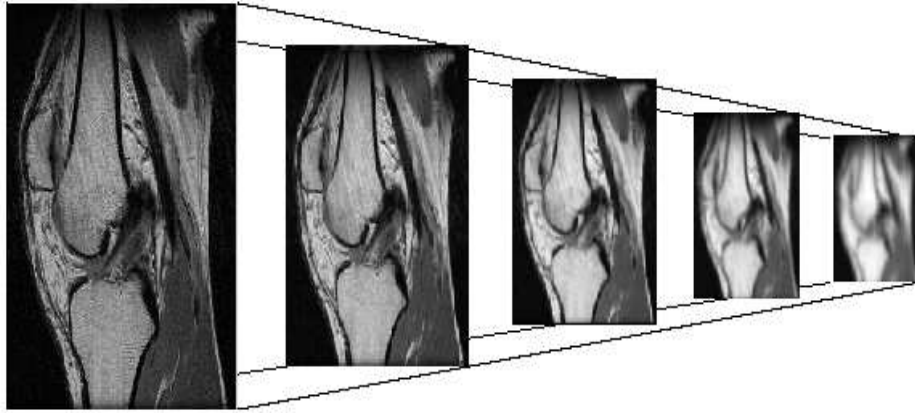


Figure 4: Gaussian Pyramid constructed from a MRI of a Human Knee. Images contain 512x512, 256x256, 128x128, 64x64 and 32x32 pixels.

The Laplacian pyramid is derived from the Gaussian pyramid and provides an interesting description of the data with a filter effect that can be used to obtain edges through a zero-crossing detection. The Laplacian is a sequence of error images  $L_0, L_1, L_2, \dots, L_N$  each being the difference between two levels of the Gaussian Pyramid:

$$L_k = g_k - EXPAND(g_{k+1}) = g_k - g_{k+1,1} \quad (8)$$

As mentioned before, the Gaussian pyramid presents a low-pass filtering effect over the images. Each successive stage of the pyramid is constructed by reducing a previous step. At each pixel, a weighted average of the neighbouring pixels is calculated. By subsampling, every successive stage of the pyramid is composed of less pixels. The inverse procedure of expansion generates an image with the same number of pixels as the previous stage of the Gaussian pyramid with a blurred effect. The difference of two images reduced and expanded up to a different stage of the pyramid corresponds to a certain level of the Laplacian pyramid, which has an overall impression of a Band Pass filter (see figure 5). The Laplacian pyramid has a Gaussian histogram centred in zero. Therefore, zero-crossings of the image can be obtain and represent edges of some features.

Pyramids and other multiple resolution techniques have been used in different image segmentation, texture and classification problems with good success (for example see [2, 4, 6, 11, 21, 36, 39]). The author believes that a multiple resolution approach can be useful in the medical image segmentation problem and will further develop the framework to use multiple resolution as a tool to be included.

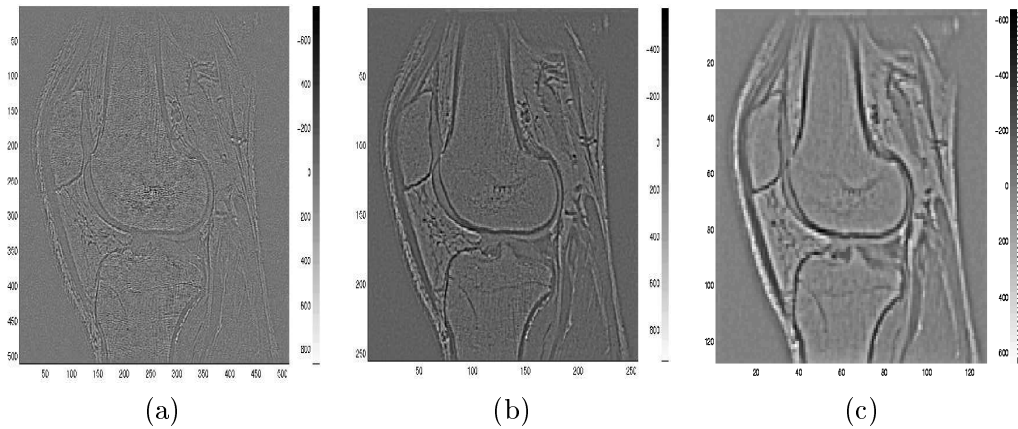


Figure 5: Three different levels of a Laplacian Pyramid constructed from a MR image slice of a human knee.

## 2.5 Texture

According to Sonka [35], the concept of texture is intuitively obvious but it has been difficult for the Image Processing community to give a satisfactory definition. Texture relates to the surface or structure of an object and depends on the relation of contiguous elements. Wilson and Spann [40] emphasise that textured regions are spatially extended patterns based on more or less accurate repetition of some unit cell, the origin of the term is related with the craft of weaving. Gonzalez [16] relates texture to other concepts like *smoothness*, *fineness*, *coarseness*, *graininess*, and describes the three different approaches for texture analysis: statistical, structural and spectral. The statistical methods rely on the moments of the grey level histogram; mean, standard deviation, skewness, flatness, etc. These can give interesting information about the image but have the drawback that there is no information about the relative position of the pixels.

Structural methods look for a basic pattern in the image, a texture element, and then describe the region according to the repetition of the pattern. The pattern can be scaled, rotated, translated, or its grey levels increased or decreased through an affine transform. In many cases this is a very powerful tool, but many images do not contain a pattern that can be repeated. In contrast, spectral methods rely on the Fourier transform of the image. Those images that present periodic structures are ideal for these methods.

Sonka stresses that texture is scale dependent, therefore a multi-scale or multiresolution analysis of an image is required if texture is going to be analysed. There is extensive research in texture analysis; Haralick [17] is a basic reference for statistical and structural approaches; MRF's are used by Cross and Jain [9] and Kervrann [25]. Keller [24] use Fractal geometry to describe texture, multiresolution approaches to

texture are used by [2, 21, 27].

Texture will be more and more important as the resolution of the MR or CT equipment increases. The current resolution already allows the texture of bone and muscle to be easily seen. Further increases in scanning resolution will reveal texture of soft tissues in a similar way that microscopes slices reveal texture of bones, cartilages, tendons or the skin. The textures encountered in MR differ greatly from synthetic textures, which tend to be structural and can be often be described with textural elements that repeat in certain patterns. MR texture exhibits a degree of granularity, randomness and, where the imaged tissue is fibrous like muscle, directionality. Thus, in general, these textures can be characterised best by statistical and spectral descriptors.

### 3 ANALYSIS OF THE DATA

The problem to be solved is to segment the human knee joint data into a set of non-overlapping regions of homogeneity corresponding to different anatomical structures. In this process, different classification and segmentation techniques will be analysed and compared to outline a suitable methodology.

The input data to this problem is a series of 87 slices of 512 x 512 pixels each one. The series of slices constitute a three dimensional volume of 512 x 512 x 87 volume elements each with a certain value of brightness that describe a human knee MR image. Even at this stage, one can easily observe that the computational burden is huge: we will have to deal with more than 22 million voxels.

#### 3.1 Grey level thresholding

A first and simple approach to segmentation of the data is to analyse the individual values of brightness of the pixels. This approach involves only the first-order features of a pixel [8] since the surrounding pixels (or voxels) are not considered to obtain higher order features. As an example, a single slice of the set is selected and displayed in figure 6(a).

The grey level histogram for the image  $\mathcal{I}$  ranges from 1 to 2787, being 1 black and 2787 white, and is defined [41] as:

$$h(g) = \frac{\#\{(k, l) \in (L_r \times L_c) : \mathcal{I}(k, l) = g\}}{\#\{L_r \times L_c\}}, g \in G \quad (9)$$

where  $\#$  denotes the number of elements in the set. The histogram (figure 6 (b)) is quite dense and although two local minima or valleys can be identified around the values of 300 and 900 using these thresholds may not be enough for segmenting the anatomical structures of the image. It can be observed that the lower grey levels, those below the threshold of 300 correspond mainly to background, which is highly noisy. The pixels with intensities between 301 and 900 roughly correspond to the region of

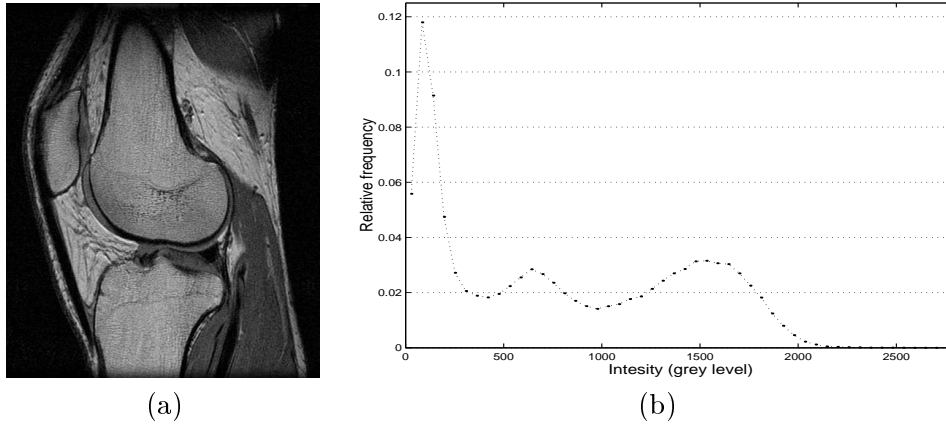


Figure 6: Human Knee Slice MRI: (a) grey level image and (b) its corresponding histogram.

muscle, but it includes parts of the skin, and the borders of other structures like bones and tissue. The upper part of the femur could be included into this region due to the inhomogeneity of the magnetic field with which the image was acquired. Many of the pixels in this grey level region correspond to transitions from one region to another. (The muscles of the thigh; Semimembranosus and Biceps Femoris in the hamstring region, do not appear as uniform as those in the calf; the Gastrocnemius, and Soleus.)

The third class of pixels with intensities between 901-2787 roughly correspond to bones - femur, tibia and patella are visible - and tissue - Infrapatellar Fat Pad, and Suprapatellar Bursa. These tissues consist of fat and serous material and have similar grey levels as the bones. The most important problem consists in Bone and Tissue sharing the same range of grey levels in this MR Image. It is therefore necessary to develop a methodology to distinguish successfully Bone and Tissue as grey level is not enough.

Some observations about the image are important. In the upper right hand side of the image, there is a discontinuity of the shape of the leg, and the very top of the image is a solid region of pixels with intensity levels lower than 300. Although these regions are not background, the inhomogeneity of the magnetic field with which the image was acquired causes the effect of background. This problem will not be addressed in this paper. Some anatomical structures like tendons, ligaments and menisci appear dark in the T1 MRI images, and therefore will be considered as background.

If the image were to be segmented using the grey level values of 300 and 900, the result would yield 3 non-overlapping sets that are presented in figure 7. Roughly the three sets contain: background for the levels 1-300, muscle for the levels 301-900 and bone and tissue for 901-2787. It is now evident that bone and tissue require a different set of descriptors in order to be differentiated.

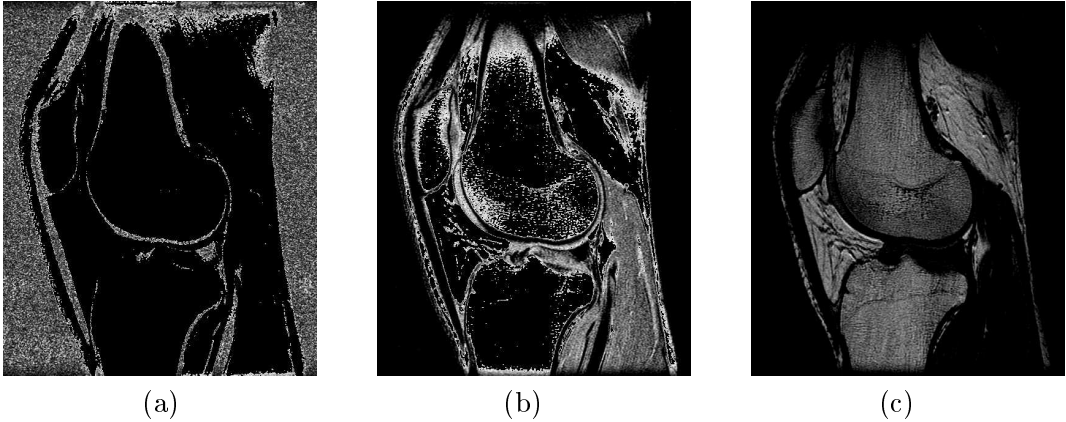


Figure 7: Three classes segmented by grey level thresholding: (a) Background, (b) Muscle and (c) Bone/Tissue.

The regions of interest in these paper are the anatomical regions of *muscle*, *bone* and *tissue* as well as the *background*. These regions were manually segmented from the image 6 (a) and their corresponding prototypes are presented in image 8 (a). The individual histograms of each of the regions are shown in figure 8 (b). As it was expected, the grey levels of bone and tissue overlap each other. Background and muscle appear quite separately and with a Gaussian shape. The inhomogeneities of the magnetic field distorts the upper part of the image and with it the histogram of muscle, that would be more bell-shaped on the lower levels

### 3.2 Standard Deviation of the grey level

The standard deviation of a neighbourhood of pixels can provide different information other than the grey level of the image. For this purpose, a neighbourhood is defined. The size of the neighbourhood can be important as it determines the scale at which the data is analysed, Sonka stresses that texture is scale dependent, therefore a multi-scale or multiresolution analysis of an image is required if texture is going to be analysed.

The mean of the intensity of the grey levels in a neighbourhood of size  $(2x+1, 2y+1)$  at coordinates  $(i, j)$  is defined by:

$$\mu = \frac{1}{(2x+1)(2y+1)} \sum_{m=-x}^x \sum_{n=-y}^y \mathcal{I}(i+m, j+n) \quad (10)$$

and the standard deviation:

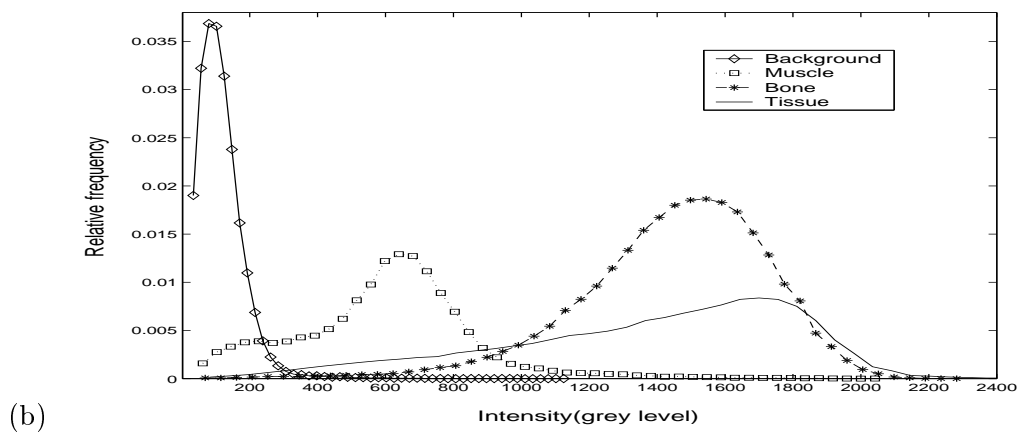
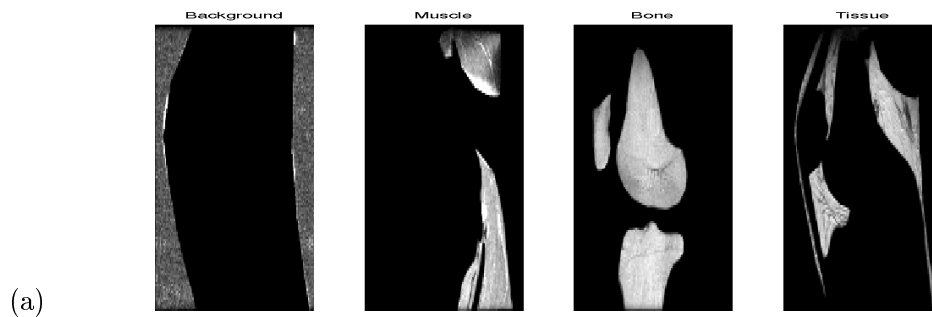


Figure 8: (a) Four manually segmented regions: Background, Muscle, Bone and Tissue, and (b) their corresponding histograms.

$$\sigma = + \sqrt{\frac{1}{(2x+1)(2y+1)-1} \sum_{m=-x}^x \sum_{n=-y}^y [\mathcal{I}(i+m, j+n) - \mu]^2} \quad (11)$$

In order to determine an adequate size of the neighbourhood from which to obtain the standard deviation of the intensities of the pixels, the stages of the Gaussian pyramid of figure 4 were analysed: the relative frequencies of the intensity levels are shown in figure 9. The level  $g_0$  of the pyramid is the original image and the relative frequencies follow those of the histogram of figure 6 (b). The results for level 1 still show a similar shape with valleys around intensity levels of 300 and 900. Level 2 shows a very different shape, the valley around 300 now shows two local minima at 200 and 400 and a local maximum around 300. This new feature is even more pronounced in level 3. This level suggest that a neighbourhood of size 8 can yield interesting results.

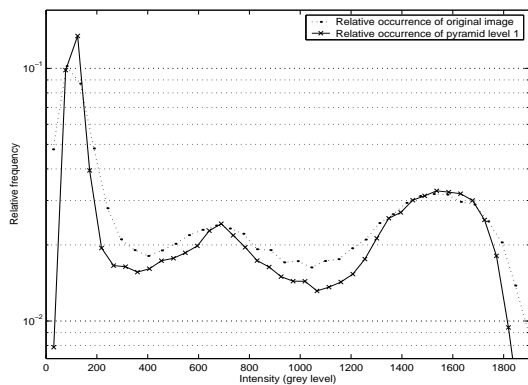
With a neighbourhood of size  $8 \times 8$  the standard deviation of the pixel intensities of figure 6 was calculated (figure 10 (a)). It is interesting to observe that the higher values of the standard deviation correspond to the transition regions, roughly, those values higher than 350 are close to the edges of bones tissue and skin. Those values lower than 350 correspond to more homogeneous regions, and account for more than 92% of the total elements. Thus, the 8% with values greater than 350 could be considered as transition regions between bone and muscle, bone and tissue or tissue and background.

### 3.3 The co-occurrence matrix

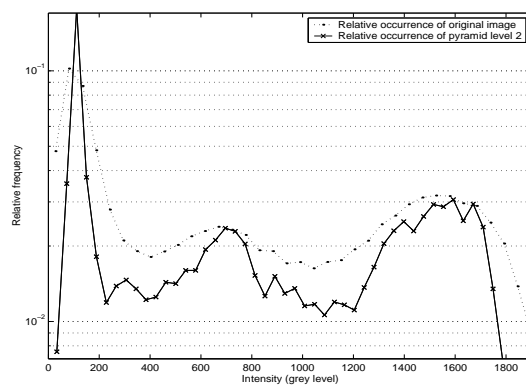
The co-occurrence matrix defines the joint occurrences of grey tones (or ranges of tones) and is constructed by analysing the grey levels of neighbouring pixels for a given image  $\mathcal{I}$ . Let the original image  $\mathcal{I}$  with dimensions for rows and columns  $N_r \times N_c$  be quantised to  $N_g$  grey levels. The co-occurrence matrix will be a symmetric  $N_g \times N_g$  matrix that will describe the number of co-occurrences of grey levels in a certain orientation and a certain pixel distance. The individual value of the unnormalised co-occurrence matrix  $P(i, j)$  will be determined by the grey levels  $i$  and  $j$  and the number of times that the grey levels appear as neighbours in the original image within a distance  $d$  and with an orientation  $\theta$ . For instance for a matrix of distance  $d = 1$  and  $\theta = 135^\circ$ :

$$P(i, j, 1, 135^\circ) = \#\{((k, l), (m, n)) \in (L_r \times L_c) \times (L_r \times L_c) \mid (k - m = 1, l - n = 1), \mathcal{I}(k, l) = i, \mathcal{I}(m, n) = j\} \quad (12)$$

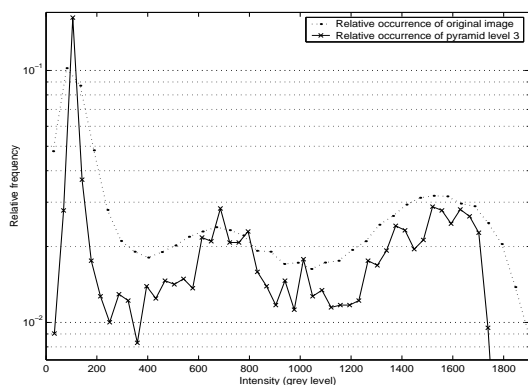
In other words, the matrix will be formed counting the number of times that to pixels with values  $i, j$  appear contiguous in the direction down-right. From this matrix different features like *entropy*, *uniformity*, *maximum probability*, *contrast*, *correlation*, *difference moment*, *inverse difference moment*, *correlation* can be calculated [17] in the following way:



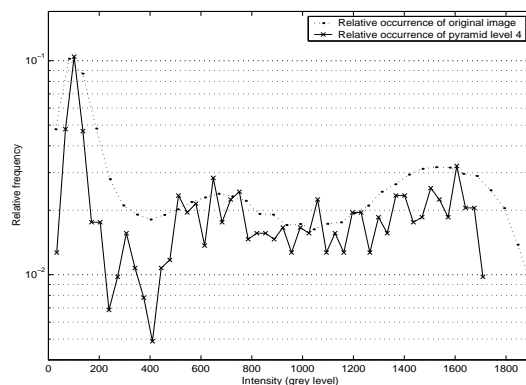
(a)



(b)



(c)



(d)

Figure 9: Relative frequencies of grey levels for four different levels of the Gaussian Pyramid presented in figure 4: (a) Level 1 (b) Level 2 (c) Level 3 (d) Level 4.

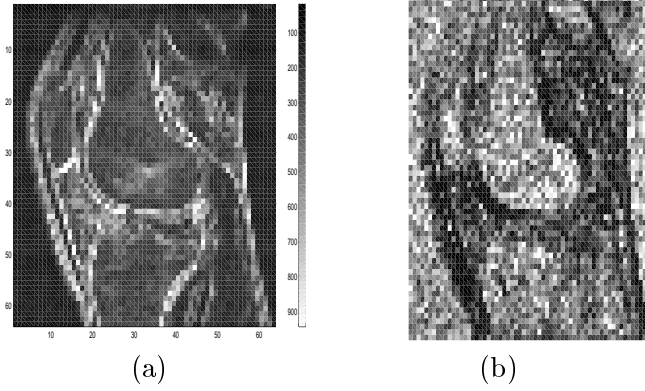


Figure 10: Descriptors of figure 6(a) calculated over an  $8 \times 8$  neighbourhood tessellation: (a) Values of Standard Deviation of the pixel intensities (b) Difference moment of order 2 of the co-occurrence matrix.

$$\textit{Uniformity or energy} \quad \sum_i \sum_j P^2(i, j) \quad (13)$$

$$\textit{Entropy} \quad \sum_i \sum_j P(i, j) \log P(i, j) \quad (14)$$

$$\textit{Maximum probability} \quad \max\{P(i, j)\} \quad (15)$$

$$\textit{Element difference moment or contrast} \quad \sum_i \sum_j |i - j|^k (P(i, j)) \quad (16)$$

$$\textit{Inverse difference moment} \quad \sum_i \sum_j \frac{P(i, j)}{|i - j|^k} \quad (17)$$

The co-occurrence matrix was calculated for neighbourhoods of size  $8 \times 8$  in the same fashion as the standard deviations were calculated. The grey levels were quantised to 8 levels or 3 quantising bits and the features of maximum probability, entropy, uniformity, difference moment of order  $k$  and its inverse were calculated. Of particular interest was the difference moment of order 2 which is presented in figure 10 (b), because the values for the tissue (Infrapatellar Fat Pad) appear to be different to the bone region.

The major disadvantage of the co-occurrence matrix is that its dimensions will depend on the number of grey levels. In many cases, the grey levels are quantised to reduce the computational cost and information is lost inevitably. Otherwise, the computational burden is huge.

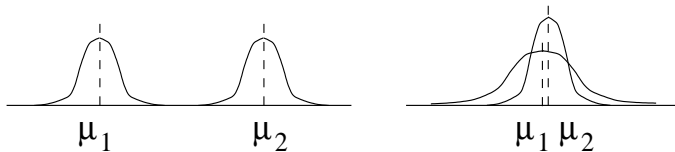


Figure 11: Bhattacharyya distance cases (a) different means with small variances (b) Similar means, different variances.

### 3.4 Bhattacharyya distance

In order to obtain a quantitative measure of *how separable* two classes are, and therefore justify the use of the third descriptor, a distance measure is required. In [8] the *Bhattacharyya distance measure* is presented as method to provide insight of the behaviour of two distributions. The variance and mean of each class are computed to calculate a distance in the following way:

$$B(i, j) = \frac{1}{4} \ln \left\{ \frac{1}{4} \left( \frac{\sigma_i^2}{\sigma_j^2} + \frac{\sigma_j^2}{\sigma_i^2} + 2 \right) \right\} + \frac{1}{4} \left\{ \frac{(\mu_i - \mu_j)^2}{\sigma_i^2 + \sigma_j^2} \right\} \quad (18)$$

where:  $B(i, j)$  is the Bhattacharyya distance between  $i$ -th and  $j$ -th classes,  
 $\sigma_i$  is the variance of the  $i$ -th class, and  
 $\mu_i$  is the grey level of the  $i$ -th class.

The first term of the distance measure depends solely of the variances of the distribution. If the variances are equal this term will be zero, and it will grow as the variances are different. The second term, on the other hand will be zero if the means are equal and is inversely proportional to the variances. If the means are different, then small variances are desired to have a large distance measure. On the other hand, if the means are similar, the variances should be significantly different in order to separate the classes. Figure 11 represents this two cases.

With the values of mean and standard deviation of the four regions within the regions of interest, the Bhattacharyya distance was calculated and the results are presented in table 3.

The important result of the values of the Bhattacharyya distance measure is the small distance between the tissue and the bone class. It is therefore necessary to include another descriptor to achieve a proper segmentation of these two classes.

To observe qualitatively the third descriptor, namely the difference moment of order 2, the scatter plots of the four selected regions were performed. The results of figure 12 (a) corresponding to the scatter plot between mean versus standard deviation are

	$\mu$	$\sigma$	Background	Muscle	Bone	Tissue
Background	91	49	0	4.36	12.51	11.70
Muscle	696	140	4.36	0	3.25	3.26
Bone	1605	212	12.51	3.25	0	0.0064
Tissue	1650	227	11.70	3.26	0.0064	0

Table 3: Mean and variance values for classes and Bhattacharyya distance

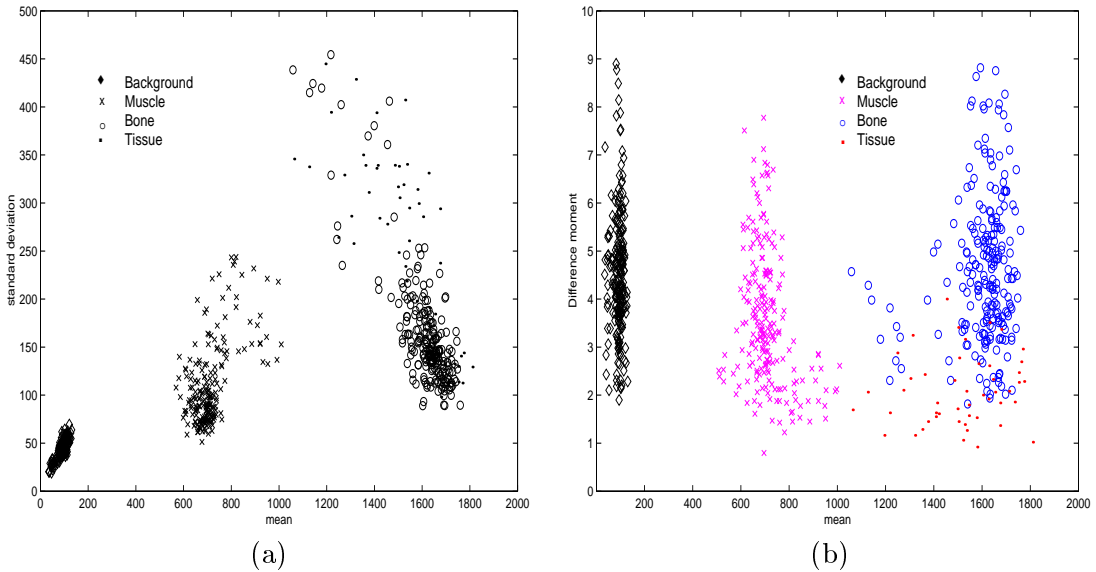


Figure 12: Scatter plots of the four selected sections: background, bone, tissue and muscle (a) Mean - Standard Deviation, (b) Mean - Difference moment of order 2.

interesting, because even though the points are only a sample of the classes, background and muscle are easily differentiable as the Bhattacharyya distance indicated. Bone and tissue appear in the same region and are not easily differentiable. In figure 12 (b), the bone appears to have a higher value of the difference moment of order 2, than that of the tissue. There is still an overlap of the classes, but many tissue points (like those with mean lower than 1200 or close to 1800) could be now separable from the bone. The values of background and muscle are spread in a similar distribution to bone, only tissue have lower values as it was previously seen in figure 10 (b).

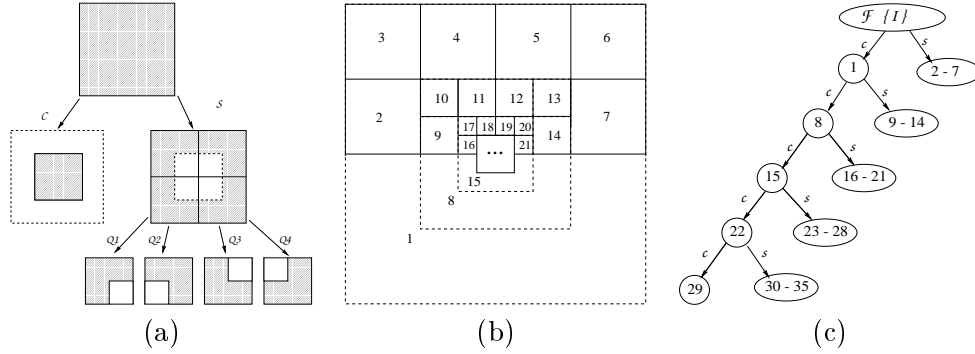


Figure 13: (a) Primitive tessellation operators and (b) Second orientation pyramid of order 3 for frequency domain tessellation used to analyse the frequency domain (c) Tree description of the regions of the pyramid.

### 3.5 A Sub-band Filtering Approach

The frequency domain presents another useful source of information even if the textures to be analysed do not present a high degree of regularity or repetition. Wilson and Spann [40] propose a set of operations that subdivide an image into smaller regions. The *quadrant operator*, which divides the image into four quadrants, and the *centre-surround operator*, which splits into an inner square region and a surrounding annulus, are illustrated in figure 13. The dimension for the quadrants are  $Q1\{1 \dots \frac{N_r}{2}, 1 \dots \frac{N_c}{2}\}$ ,  $Q2\{1 \dots \frac{N_r}{2}, \frac{N_c}{2} + 1 \dots \frac{N_c}{2}\}$ ,  $Q3\{\frac{N_r}{2} + 1 \dots \frac{N_r}{2}, 1 \dots \frac{N_c}{2}\}$ ,  $Q4\{\frac{N_r}{2} + 1 \dots \frac{N_r}{2}, \frac{N_c}{2} + 1 \dots \frac{N_c}{2}\}$ , and for the centre-surround  $c\{\frac{N_r}{2} + 1 - \frac{N_r}{x} \dots \frac{N_r}{2} + \frac{N_r}{x}, \frac{N_c}{2} + 1 - \frac{N_c}{x} \dots \frac{N_c}{2} + \frac{N_c}{x}\}$ ,  $s\{\mathcal{I} - c\}$ . Where  $x$  determines the dimensions of the inner centre, if  $x = \frac{1}{4}$ , the width of the centre is one half of the original image. It will be assumed that  $N_r = 2^a$ ,  $N_c = 2^b$  so that the results of the divisions are always integer values.

Combining the operators in diverse combinations and order can yield different tessellations, as the well known Gaussian and Laplacian Pyramids. For this work, the Second Orientation Pyramid presented in figure 13(a) was selected for the tessellation of the frequency domain. The main hypothesis to be tested is that the different structures to be segmented contain different frequencies and orientation, specially between tissue and bone.

Wilson and Spann proposed the following steps to obtain the feature image components of a given image  $\mathcal{I}$ :

1. Calculate the Fourier transform of the image  $\mathcal{I}_\omega = \mathcal{F}\{\mathcal{I}\}$
2. Multiply the transformed image by a window function (a Gaussian instead of a f.p.s.s. will be used) corresponding to the  $j$ -th region  $\mathcal{I}_\omega \mathcal{G}_j$
3. Inverse transform the data  $\mathcal{F}^{-1}\{\mathcal{I}_\omega \mathcal{G}_j\}$

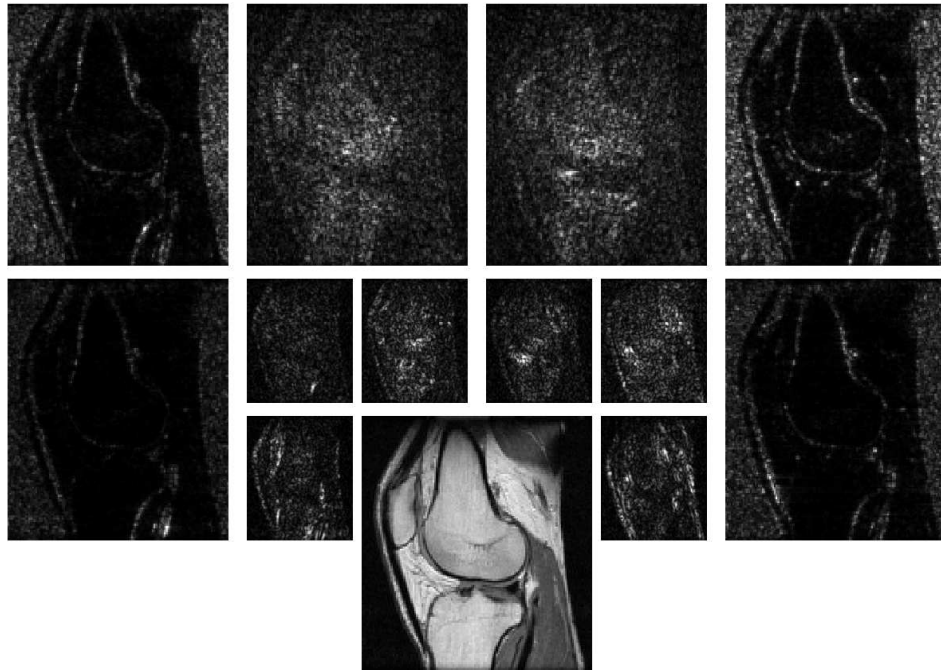
Each region of the tessellation yields a result according to the previous procedure, the regions corresponding to the first two levels of the pyramid, tessellations 2 to 14 are presented in figure 14 (a). The first observation is the high pass nature of the background of the image in regions number 2, 3, 6 and 7. It was expected that the background would be mainly noise and therefore of high frequency in nature. Region 8 is a low pass filtered I. The other regions, also of high frequency, have their higher intensities equally in bone, tissue and muscle, which might characterise its texture in other levels. In figure 14 (b) The fourth level of the pyramid, regions 23 to 35 are presented. The higher intensities are now distributed among the different structures depending on the frequencies and orientation of each section.

## 4 COMPARATIVE RESULTS

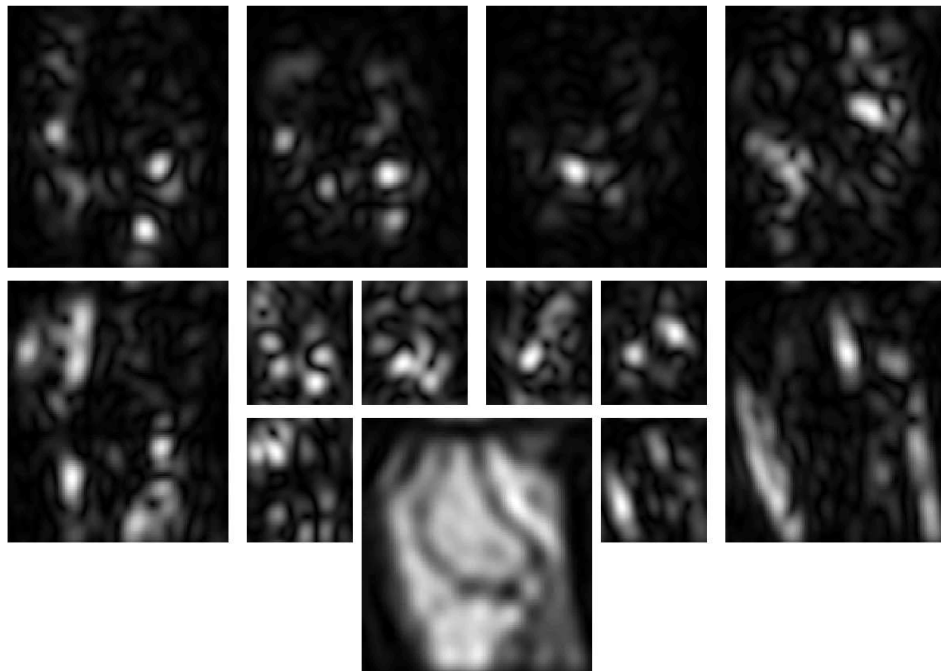
With the objective of segmenting the three anatomical structures, namely, muscle, tissue and bone, as well as the background of the image, the average values of the four previously determined hand segmented regions were considered as initial conditions. A K-means segmentation algorithm as described in [30] and proposed by [28] was implemented. In the first case, the descriptors: mean, standard deviation and difference order moment of order 2 of the co-occurrence matrix were obtained for three different scales using tessellations of sizes  $4 \times 4$ ,  $8 \times 8$ , and  $16 \times 16$ . The nine features were used in a classification. The classes, as in the further classifications, are represented by the following intensity values: 1 background, 2 muscle, 3 bone, and 4 tissue. Figure 15 (a) presents the results. In figure 15 (b) the individual structure classes are presented: Transition, Muscle, Bone and Tissue. Two important observations should be noted. First, the tissue region under the patella and next to the femur, that has the same grey level intensity as the bones: femur, tibia and patella, is now separated into a different class. Second, the results appear in mosaics and not as sharp in the borders of structures due to the tessellations used to calculate the features. It is evident that the upper region of the image is misclassified due to the inhomogeneity of the magnet during the MRI acquisition process.

The frequency sub-band filtering approach yields similar results when classifying with k-means. The first classification was done with regions 1 to 7, the second with region 2 to 14, the third with 2 to 21 without 8, and so on, adding 6 regions at each level. The classifications for the first five levels were calculated and figure 16 presents the results for levels 1, 3, 5. The results are interesting, in the first level of the pyramid, there are not enough elements to clearly distinguish bone and tissue, but as the levels increase, these regions become more uniform and smooth. On the other hand, the first classification still keeps very fine details, like the cartilage between the femur and the infrapatellar pad.

In order to compare numerically the different figures a simple error metric was calculated counting the number of pixels that were correctly classified, according to the hand segmented masks of figure 8 (a) and dividing them over the number of pixels



(a)



(b)

Figure 14: Two separate levels of the Second Orientation Pyramid, each containing 13 Regions: (a) first two levels of the Second Orientation Pyramid, regions 2 to 14, (b) third and fourth level, regions 23 to 35. .

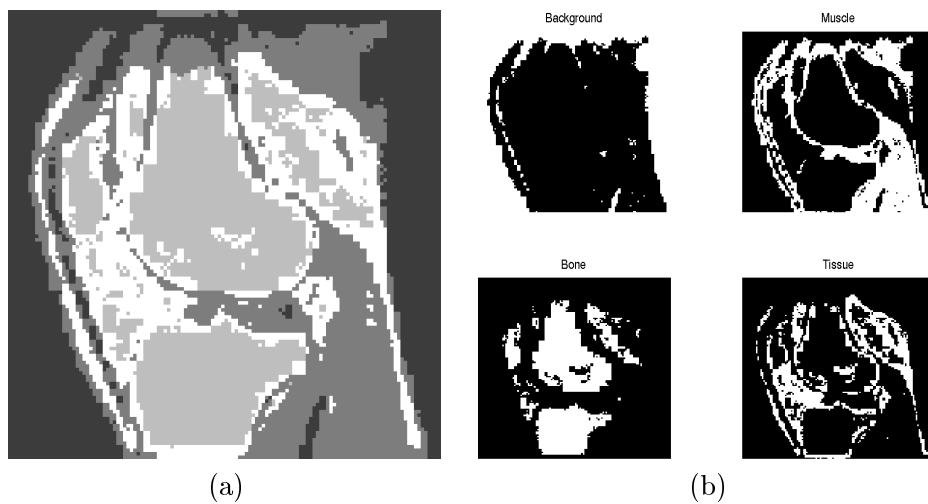


Figure 15: K-means classification of MR image of a human knee based on 9 parameters: mean, standard deviation and difference order moment of order 3 of the co-occurrence matrix of three tessellations of size  $4 \times 4$ ,  $8 \times 8$  and  $16 \times 16$ . (a) Four classes represented by intensity values: 1 - background, 2 - muscle, 3 - bone and 4 - tissue. (b) Four classes individually presented.

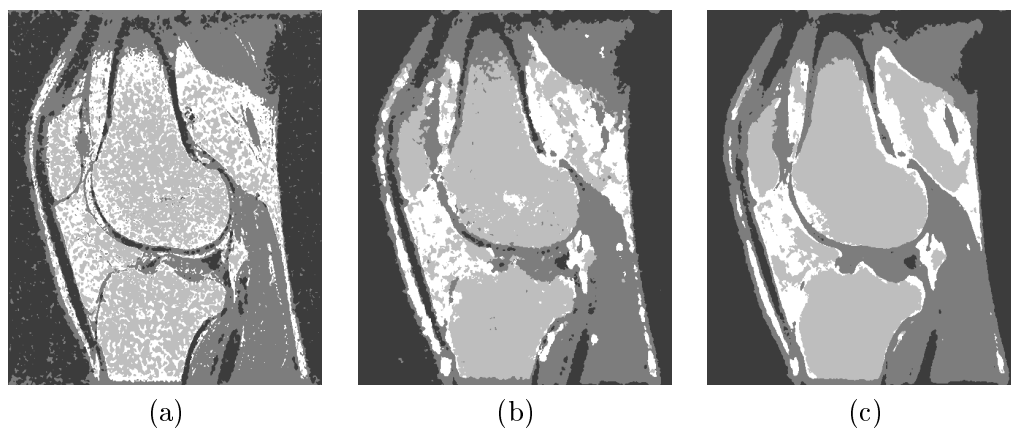


Figure 16: K-means classification of MR image of a human knee based on frequency and orientation regions from (a) First level of the Second Orientation Pyramid (b) Second level of the Second Orientation Pyramid (c) Third level of the Second Orientation Pyramid.

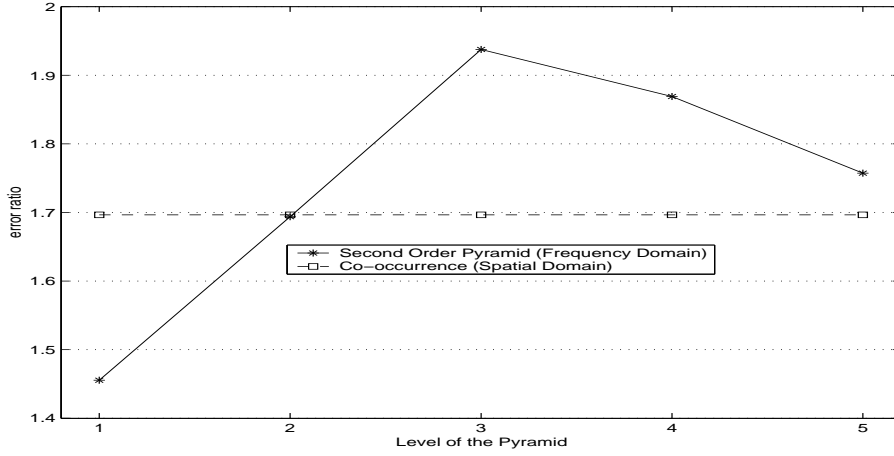


Figure 17: Error ratio comparison between Frequency domain sub-band filtering and Spatial domain features, co-occurrence matrix, variance and mean.

misclassified.

$$e = \frac{\sum_{i=1}^n \#\{(k, l) \in (L_r \times L_c) \mid (k, l) \in C_i \cap (k, l) \in M_i\}}{\sum_{i=1}^n \#\{(k, l) \in (L_r \times L_c) \mid (k, l) \in C_i \cap (k, l) \in M_i^c\}} \quad (19)$$

where:  $e$  is the error ratio of correctly classified and missclassified pixels,

$n$  the number of classes, in this case  $n = 4$ ,

$C_i$  the  $i$ -th class,

$M_i$  the  $i$ -th Mask, and

$M_i^c$  the complement of the  $i$ -th Mask.

The error ratio for the first five levels of the Pyramid was compared against the error ratio of the results for the co-occurrence matrix method. Figure 17 presents this comparison. The maximum error ratio corresponds to the third level of the pyramid, and from this level, the pyramid method is better than the co-occurrence method.

## 5 FUTURE WORK

In the previous sections two classification schemes were performed over one single MR image of a human knee. It can be observed that the segmentation of medical images into anatomical structures is not an easy task that can be tackled by one simple algorithm. In many cases, the specific clinical problem at hand may define the proper approach. Careful analysis of the data, research of the current methods and

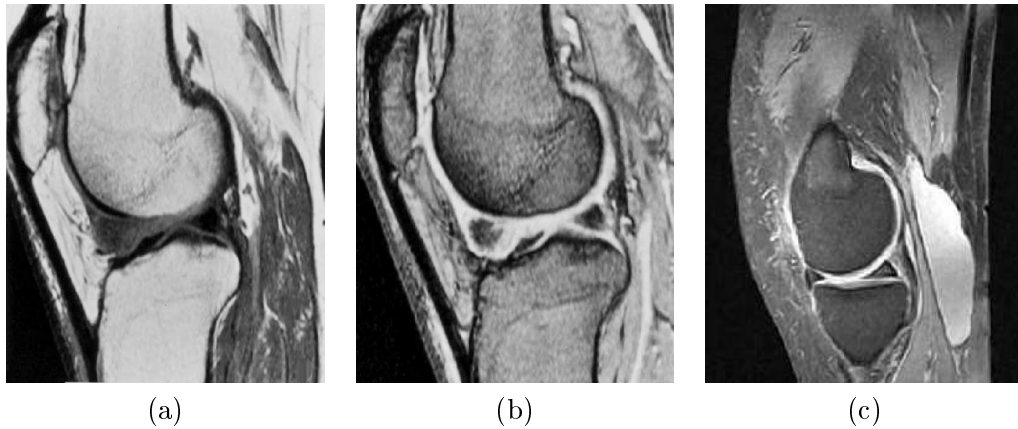


Figure 18: T1, T2 and PD MR Images of a human knee.

techniques and extensive experiments will have to be carried out in order to propose a robust flexible framework for segmentation of MR data.

In order to develop a more robust segmentation framework several improvements are required. Some of them could be the combination of:

- Correction or compensation of the inhomogeneities of the magnetic field in the image.
- Use of multispectral information in the different weighting methods of MRI
- Use of Gradient (Edge) information.
- Analysis of the data in the frequency domain.

It is very important that a correction or compensation for the inhomogeneities of the magnet can be obtained. Wells [38] propose a method of correction of the magnetic field while obtaining the segmentation of the images through adaptive segmentation. Dawant [12] proposes other methods for correction of a bias field that depend on several hand picked points over the image. Both methods should be analysed to obtain a better result.

Another improvement is to incorporate the different contrast sequences that are possible with Magnetic Resonance Imaging process. A single tissue can appear quite differently in T1, T2 and PD images. Figure 18 show examples of these three weighting methods. While the cartilage region that surrounds the condyles appears dark in the T1 image, is looks bright in the T2 image. The bone that appears bright in the T1 image appears dark in the PD image. Three parallel sets of T1, T2 and Proton Density images of the same region with the same acquisition parameters would be required to process them as it is done in *colour* segmentation.

## 6 CONCLUSIONS

In this work a human knee image acquired through Magnetic Resonance was analysed and segmented. First the histogram was analysed and used for a simple classification by thresholding. Then, by the use of three descriptors of the data, namely, intensity, standard deviation and a difference order moment of the co-occurrence matrix. The segmentation was improved and five classes could be distinguished: background, muscle, bone and tissue and a transition class with a certain degree of success.

The first conclusion of the present work is that the task of segmentation of Magnetic Resonance Images is not straightforward. The task is even more complicated since anatomical structures are not regular having variable and complex shapes, non-periodic textures, and artifacts and inhomogeneities due to the acquisition of the images. Even if the magnet inhomogeneities are corrected, the proper selection of a series of descriptors of the data that can differentiate successfully the anatomical structures is non-trivial. So far, intensity, standard deviation, co-occurrence matrix and frequency domain orientation have been considered to be of use in the description of the data.

The incorporation of edges and texture to determine “what” is “where” also presents a further development that could be very useful. The edge information obtained through the zero-crossing could help to determine the precise boundary location between two classes.

Different classification schemes must be studied to determine the best for the given tasks. Here only K-means was considered, but others like Expectation Maximisation could be used. Wells [38] proposed a classification method that takes into account inhomogeneities of magnetic field and determines a “bias” map while doing the classification incorporating into the image model could prove fruitful.

The results presented in this report consist solely of two dimension images. The extension to three dimensions could be done easily in some cases, but in others, is less obvious or practical. Texture in three dimensions is an interesting and important area of research which we hope to study further.

## References

- [1] AAOS. News release: 6 million a year seek medical care for knees. *American Academy of Orthopaedic Surgeons*, <http://orthopedics.about.com/gi/dynamic/offsite.htm?site=http://www.aaos.org/wordhtml/press/trend.htm>, 1997.
- [2] Charles Bouman and Bede Liu. Multiple resolution segmentation of textured images. *IEEE Transactions on Pattern Analysis and Machine Intelligence*, PAMI-13(2):99–113, 1991.
- [3] Peter J. Burt and Edward H. Adelson. The laplacian pyramid as a compact image code. *IEEE Trans. on Communications*, 31(4):532–540, 1983.

- [4] Andrew Calway. *The Multiresolution Fourier Transform: A General Purpose Tool for Image Analysis*. PhD thesis, Department of Computer Science, The University of Warwick, September 1989.
- [5] John Canny. A computational approach to edge detection. *IEEE Transactions on Pattern Analysis and Machine Intelligence (PAMI)*, 8:679–698, 1986.
- [6] Guo-Huei Chen and Roland Wilson. Image segmentation based on the multiresolution fourier transform and markov random fields. Technical Report CS-RR-351, Dept. of Computer Science, University of Warwick, Coventry, UK, 1998.
- [7] Jean-Pierre Renard Claude Reyraud and Christine Blondel. Le magnétisme. *La Recherche, Spécial*(Août/septembre/octobre):50–53, 2001.
- [8] Guy B Coleman and Harry C Andrews. Image segmentation by clustering. *Proceedings of the IEEE*, 67(5):773–785, 1979.
- [9] George R. Cross and Anil K. Jain. Markov random field texture models. *IEEE Transactions on Pattern Analysis and Machine Intelligence*, PAMI-5(1):25–39, 1983.
- [10] James E Crouch and Robert McClintic. *Human Anatomy and Physiology*. John Wiley & Sons, NY, 1971.
- [11] Andrew Davies and Roland Wilson. Linear feature extraction using the multiresolution fourier transform. Technical Report CS-RR-170, Dept. of Computer Science, University of Warwick, Coventry, UK, 1990.
- [12] Benoit Dawant, Alex Zijdenbos, and Richard Margolin. Correction of intensity variations in mr images for computer aided tissue classification. *IEEE Transactions on Medical Images*, 12(4):770–781, 1993.
- [13] Steve Webb ed. *The Physics of Medical Imaging*. Institute of Physics Publishing, Bristol, 1996.
- [14] Jim Feeney. Magnetic resonance imaging - a window into the human body. *Mill Hill Essays*, <http://www.nimr.mrc.ac.uk/MillHillEssays/1996/mri.htm>, 2001.
- [15] M.A. Foster. *Magnetic Resonance in Medicine and Biology*. Pergamon Press, New York, 1984.
- [16] Rafael C. Gonzalez and Richard E Woods. *Digital Image Processing*. Addison Wesley, Reading Mass, second edition, 1992.
- [17] Robert M. Haralick. Statistical and structural approaches to texture. *Proceedings of the IEEE*, 67(5):786–804, 1979.
- [18] Karsten Held, Elena Rota Kops, Bernd J Krause, William M Wells, Ron Kikinis, and Hans-Wilhelm Muller-Gartner. Markov random field segmentation of brain MR images. *IEEE Transactions on Medical Imaging*, 16:6, 1997.
- [19] Jacek Hennel, Teresa Kryst-Widzowska, and Jacek Klinowski. *A Primer of Magnetic Resonance Imaging*. Imperial College Press, London UK, 1997.
- [20] Joseph P. Hornak. *The Basics of MRI*. World Wide Web, <http://www.cis.rit.edu/htbooks/mri/bmri.htm>, 1996.

- [21] Tao-I Hsu, Andrew Calway, and Roland Wilson. Analysis of structured texture using the multiresolution fourier transform. Technical Report CS-RR-226, Department of Computer Science, The University of Warwick, 1992.
- [22] Tina Kapur. *Model based three dimensional Medical Image Segmentation*. PhD thesis, AI Lab, Massachusetts Institute of Technology, May 1999.
- [23] J. Alex Becker Keith A. Johnson. *The Whole Brain Atlas*. World Wide Web, <http://www.med.harvard.edu/AANLIB/home.html>, 1999.
- [24] James M Keller and Susan Chen. Texture description and segmentation through fractal geometry. *Computer Vision, Graphics and Image Processing*, 45:150–166, 1989.
- [25] Charles Kervrann and Fabrice Heitz. A markov random field model-based approach to unsupervised texture segmentation using local and global spatial statistics. *IEEE Transactions on Image Processing*, 4(6):856–862, 1995.
- [26] Tony Lindeberg. Scale-space theory: A basic tool for analysing structures at different scales. *Journal of Applied Statistics*, 21(2):225–270, 1994.
- [27] M. Eden M. Unser. Multiresolution feature extraction and selection for texture segmentation. *IEEE Transactions on Pattern Analysis and Machine Intelligence*, 11(7):717–728, 1989.
- [28] J. MacQueen. Some methods of classification and analysis of multivariate observations. In L.M. LeCam and J Neyman, editors, *Fifth Berkeley Symposium on Mathematical Statistics and Probability*, pages 281–297, Berkeley, CA, 1967.
- [29] D Marr and E. Hildreth. Theory of edge detection. *Proc. R. Soc. London*, B207:169–182, 1980.
- [30] Jose L. Marroquin and Federico Girosi. Some extensions of the K-means algorithm for image segmentation and pattern classification. Technical Report AIM-1390, AI Lab, Massachusetts Institute of Technology, 1993.
- [31] Samuel K. Moore. Better breast cancer detection. *IEEE Spectrum*, 38(5):50–54, 2001.
- [32] Inc NEC Research Institute. *ResearchIndex NECI Scientific Literature Digital Library*. World Wide Web, <http://citeseer.nj.nec.com/source.html>, 2001.
- [33] Nikhil R. Pal and Sankar R. Pal. A review on image segmentation techniques. *Pattern Recognition*, 26(9):1277–1293, 1993.
- [34] Azriel Rosenfeld and Larry S. Davis. Image segmentation and image analysis. *Proceedings IEEE*, 67(5):764–772, 1979.
- [35] Milan Sonka, Vaclav Hlavac, and Roger Boyle. *Image Processing, Analysis and Machine Vision*. PWS, Pacific Grove, USA, second ed. edition, 1998.
- [36] P. Summers, A. Bhalerao, and D. Hawkes. Multi-resolution, model based segmentation of MR angiograms, 1997.
- [37] Jasjit S. Suri. Two-dimensional fast magnetic resonance brain segmentation. *IEEE Engineering in Medicine and Biology*, 20(4):84–95, 2001.
- [38] W.M. Wells, W.E.L. Grimson, R. Kikinis, and F.A. Jolesz. Adaptive segmentation of MRI data. *IEEE Transactions on Medical Imaging*, 15(4):429–442, 1996.

- [39] Roland Wilson and Chang-Tsun Li. Multiresolution random fields and their application to image analysis. Technical Report CS-RR-361, Dept. of Computer Science, University of Warwick, Coventry, UK, 1999.
- [40] Roland Wilson and Michael Spann. *Image Segmentation and Uncertainty*. John Wiley and Sons Inc., New York, 1988.
- [41] Gerhard Winkler. *Image Analysis, Random Fields and Dynamic Monte Carlo Methods*. Springer, Berlin, Germany, first ed. edition, 1995.
- [42] Y. Zhang, M. Brady, and S. Smith. Segmentation of brain MR images through a hidden markov random field model and expectation maximization algorithm. *IEEE Trans. Medical Imaging*, 20(1):45–57, 2001.